



A Combined experimental and theoretical study of the accelerated hydrogen evolution kinetics over wide pH range on porous transition metal doped tungsten phosphide electrocatalysts

Jiajun Wang^{a,c,1}, Kuan Chang^{b,c,1}, Zeyu Sun^a, Ji Hoon Lee^c, Brian M. Tackett^c, Cheng Zhang^d, Jingguang G. Chen^{c,*}, Chang-Jun Liu^{a,*}

^a Collaborative Innovation Center of Chemical Science and Engineering, School of Chemical Engineering and Technology, Tianjin University, Tianjin 300072, PR China

^b Department of Chemical Engineering, Tsinghua University, Beijing, 100084, PR China

^c Department of Chemical Engineering, Columbia University, 500 W. 120th St., New York, NY 10027, United States

^d Department of Chemistry, Long Island University Post, Brookville, New York 11548, United States



ARTICLE INFO

Keywords:

Hydrogen evolution reaction
Water dissociation
Density functional theory
Transition metal doping
Electrochemistry

ABSTRACT

Modifying the nanostructures and chemical compositions provides an opportunity of developing the effective and inexpensive hydrogen evolution reaction (HER) electrocatalysts. Herein, porous transition metal doped tungsten phosphide (M-WP, M=Mo, Co) catalysts have been developed as enhanced HER electrocatalysts in comparison with pristine WP. Owing to the incorporated transition metals, the as-prepared M-WP nanomaterials exhibit porous nanostructures, abundant active sites and reduced charge transfer resistances. Density functional theory (DFT) calculations further demonstrate that the Co dopant simultaneously facilitates the water dissociation step and optimizes the hydrogen adsorption free energy during the entire HER process. Consequently, the Co-WP catalyst shows efficient and stable HER performance over wide pH range. This work demonstrates how metal dopants promote the HER kinetics and develops the strategy for further designing non-precious metal based nanomaterials for energy conversion and electrocatalysis.

1. Introduction

With the growing concerns about fossil fuel depletion and environmental pollutions, global efforts have been stimulated to develop clean and renewable energy [1,2]. Hydrogen is a green fuel with high energy density and has been considered as a promising candidate for replacing traditional fossil fuels [3,4]. However, current hydrogen generation primarily relies on the coal gasification or steam methane reforming processes, which causes the intensive energy consumption and CO₂ release as a by-product [5,6]. In recent years, the hydrogen evolution reaction (HER) from water splitting, which realizes a sustainable and environmental friendly hydrogen generation when electrons are obtained from renewable sources, has drawn increasing attention [7–9]. Although platinum-based catalysts are the best known HER catalysts, the limited abundance and high cost still hinder their large-scale applications. Therefore, various earth-abundant and cost-effective HER catalysts have been explored [10–12]. On the other hand, it is well known that HER mechanisms significantly change with

different pH environments [13]. Usually, HER rates in acid environments are superior to those in alkaline and neutral solutions, as a large amount of protons (H⁺) in acid solutions should facilitate the HER process for thermodynamic and kinetic reasons [13,14]. However, the pH values can be different in practical applications [9,15–18]. For example, currently large-scale water electrolysis is usually performed in basic media, while in the proton exchange membrane (PEM) technology the water-splitting devices are often carried out in acidic and neutral media [9,16]. Meanwhile, numerous non-precious metal oxygen evolution reaction (OER) catalysts usually only perform well in alkaline electrolytes [5,17]. Therefore, it is very critical to further develop efficient non-precious metal catalysts that can be applied over wide pH range.

Currently, transition metal phosphides (TMPs) have exhibited intrinsically good electrical conductivity and shown efficient HER performances in acid environments [19–25]. Tungsten phosphides have been known as acid HER catalysts, but very few studies reported their HER performances in neutral or alkaline environments [26–28].

* Corresponding authors.

E-mail addresses: jgchen@columbia.edu (J.G. Chen), ughg_cjl@yahoo.com (C.-J. Liu).

¹ These authors contributed equally to this work.

Recently, it has been demonstrated that dopants on transition metal sulfides and selenides modified the structures and charge transfer resistance, leading to an enhanced acid HER performance [29,30]. Therefore, developing novel tungsten phosphide-based nanomaterials, with metal doping strategy, might facilitate their HER kinetics over wide pH range. Moreover, DFT calculations often provide insights into the electrocatalysts design with enhanced properties [5,31]. Previous DFT results have shown that the metal dopants help to optimize the hydrogen adsorption free energy (ΔG_{H^+}), which is a key factor for describing the acid HER activities [7,32]. However, at the beginning of HER process in alkaline or neutral cases, the water dissociation step makes the overall HER process slow [13,17]. It is therefore necessary to clarify the effect of metal dopants on the entire HER reaction network. In this work, transition metals (Mo and Co) have been doped into pristine WP using a simple and safe method, leading to the formation of novel porous M-WP (M = Mo, Co) nanomaterials. Compared with the undoped WP, the as-prepared M-WP nanomaterials exhibit numerous advantages: higher surface areas, more porous nanostructures, more exposed active sites and lower resistance for charge transfer. In parallel, DFT calculations demonstrate that the Co dopants synergistically enhance the water dissociation rate and optimize hydrogen adsorption free energy during the entire HER process. Consequently, the Co-WP catalyst exhibits efficient HER activity and stability over wide pH range (i.e. 1.0 M KOH, 0.5 M H_2SO_4 and 1.0 M PBS), which are significantly improved over those of undoped WP. This work shows the effect of metal dopants on HER process and provides insights in developing non-precious metal electrocatalysts using the metal doping method.

2. Experimental section

2.1. Synthesis

Typically, for the synthesis of Mo-WP, a certain amount of ammonium tungsten oxide hydrate ($(NH_4)_6W_{12}O_{39} \cdot xH_2O$), ammonium molybdate tetrahydrate ($(NH_4)_4Mo_7O_{24} \cdot 4H_2O$), citric acid monohydrate ($C_6H_8O_7 \cdot H_2O$) and ammonium hypophosphite ($NH_4H_2PO_2$) were dissolved in water with a molar ratio of 0.95: 0.05: 2: 1 (W: Mo: citric acid: P). The solution was kept at 90 °C for 12 h and then dried at 120 °C. The dried sample was then calcined at 500 °C for 10 h. The calcined samples were ground and reduced under H_2/Ar (H_2 : 10 ml/min, Ar: 20 ml/min) at 650 °C for 2 h with a heating rate of 2 °C/min. And then the sample was cooled down to room temperature under Ar protection. The final product was denoted as Mo-WP. For the synthesis of Co-WP, the molybdenum salt was replaced by cobaltous carbonate basic ($Co_3(OH)_6(CO_3)_2$) and the moral ratio of W/Co was also 0.95: 0.05. The subsequent procedures were the same as Mo-WP. Pristine WP, MoP and CoP were also prepared with the corresponding transition metal salts, other procedures were the same as that of Mo-WP. In particular, the theoretical metal dopant atomic percentage is 5 at% Co-WP and 5 at% Mo-WP. For varying the Mo/Co dopants atomic percentages, the ratios of different precursors were changed in accordance with the designed ratios.

2.2. Electrochemical measurements

The electrochemical measurements were carried out in a typical three-electrode cell using a CHI 660C workstation at room temperature. A graphite rod was used as the counter electrode. An Ag/AgCl (KCl) electrode was used as the reference electrode in 1 M KOH and 1 M phosphate buffer saline (PBS) electrolytes, respectively. A saturated Hg/Hg_2SO_4 (K_2SO_4) electrode was used as the reference electrode in 0.5 M H_2SO_4 . The reference electrodes have been calibrated in an H_2 saturated electrolyte with respect to an *in-situ* reverse hydrogen electrode (RHE) via using platinum wires as working electrodes. Linear scan voltammetry (LSV) was carried out at a scan rate of 2 mV s⁻¹ in electrolytes with the electrode rotating at a rate of 2000 rpm. All results

were revised by ohmic potential drop (iR) correction. The stability tests were performed in the electrolytes at room temperature at a sweep rate of 50 mV s⁻¹ for 2000 cycles. The AC impedance spectroscopy measurements were carried out in 0.5 M H_2SO_4 and 1 M KOH at an overpotential of −160 mV in the frequency range of 10² to 10⁵ Hz. Prior to all the above measurements, the electrolyte solution was purged by N_2 for 30 min.

In a typical working electrode preparation procedure, Co-WP (4.0 mg) was dispersed in 1 ml of aqueous solution of 0.5% Nafion via ultrasonic dispersion for 30 min to obtain a homogeneous ink. Then 10 μ L of the ink (containing 40 μ g catalyst) was loaded onto a glassy carbon electrode (GCE) of 5 mm in diameter (loading amount: 0.20 mg cm⁻²). The catalyst modified GCE was then dried at room temperature. The GCEs were also modified with other materials with the same catalyst loading.

2.3. Characterizations

X-ray diffraction (XRD) patterns of as-prepared samples were recorded on a Rigaku D/MAX-2500 V/PC diffractometer. Scanning electronic microscopy (SEM) investigations were performed on an FEI NanoSEM 430. Transmission electron microscopy (TEM) measurements were performed on a Philips Tecnai G2F20 system with an EDX to determine bulk atomic concentrations, operated at 200 kV. Before the measurements, samples were suspended in absolute methanol for 30 min. After standing for 20 min, the supernatant solution was dropped onto a copper grid. Nitrogen adsorption-desorption isotherms were recorded via a Micromeritics TriStar 3000 instrument. Specific surface areas of as-prepared samples were measured with the Brunauer – Emmett – Teller (BET) equation and pore size distributions were calculated via the Barrett – Joyner – Halenda (BJH) formula. The actual Co and Mo atomic percentages were determined by the inductively coupled plasma optical emission spectroscopy (ICP-OES), which were performed by Varian VISTA-MPX.

2.4. DFT calculations

Density functional theory (DFT) calculations were carried out using the Vienna Ab-initio Simulation Package (VASP) package [33]. The generalized gradient approximation (GGA) with the Perdew-Burke-Ernzerhof (PBE) functional was adopted to describe the electronic exchange and correlation effects [34]. Spin-polarization was included for all calculations. Van der Waals correction was included in the calculation using DFT-D2 method of Grimme [35]. To accelerate SCF convergence, a Gaussian smearing technique was adopted with a smearing parameter of $k_B T = 0.1$ eV for slabs and 0.01 eV for molecules for the fractional occupation of the one-electron energy levels. All calculated values of energy were then extrapolated to $k_B T = 0$.

In the calculations, the surface was simulated with a three-layers thick $p(4 \times 4)$ (011) plane of WP unit slab with ~30 Å vacuum. A Monkhorst – Pack k-point net of $3 \times 3 \times 1$ was chosen to sample the reciprocal space for the slab calculations, whereas only the gamma point was sampled for the molecule calculations. The simulation was run with a cutoff energy of 400 eV throughout the computations.

For all studied structures, Gibbs free energy was calculated by the formula $\Delta G = \Delta E + \Delta ZPE - \Delta S$, where zero point energy change and entropy correction were determined by frequency calculation. Adsorption energy $\Delta E_{(^\ddagger H)}$ was calculated by subtracting the energies of gas phase species and clean surface from the total energy of the absorbed system, i.e., $\Delta E_{(^\ddagger H)} = E_{(^\ddagger H)/slab} - (0.5H_2 + E_{slab})$ and a more negative ΔE_{ads} indicates a more stable adsorption. To evaluate the energy barrier, the transitional state (TS) was determined using the climbing image nudged elastic band (CI-NEB) method combined with the dimer method. The energy barrier and reaction energy were calculated according to $E_{ads}^\ddagger = E_{TS} - E_{IS}$ and $E_{ads} = E_{FS} - E_{IS}$. E_{IS} , E_{FS} and E_{TS} were the energies of the corresponding initial state (IS), final state (FS), and

transition state (TS), respectively.

3. Results and discussion

3.1. Characterizations of catalysts

X-ray diffraction (XRD) is performed to investigate the structures of the as-prepared catalysts (shown in Fig. S1a). The pristine WP nanostucture is well-indexed into an orthorhombic structure (JCPDS card no. 29-1364). The intense and sharp diffraction peaks at 28.66° , 31.04° and 42.94° match well with the (002), (011) and (202) reflections of orthorhombic WP, indicating a pure phase and a high crystallinity. For the M-WP (M = Mo, Co) nanomaterials, no new peaks appear after the incorporation of Mo or Co, suggesting the homogeneous incorporation of Mo or Co into the lattice of WP [7,36]. Moreover, compared with pristine WP, both Mo-WP and Co-WP show slight diffraction peak shifts, indicating the lattice parameter change induced by transition metal doping and confirming the formation of metal-doping structure [7]. Moreover, as shown in Fig. S2, both Co-WP and Mo-WP exhibit similar Raman and FTIR spectra with those of WP, consistent with the formation of metal-doping compounds. [37] For comparison, XRD patterns of pristine MoP (JCPDS card no. 24-0771) and CoP (JCPDS card no. 29-0497) are shown in Fig. S1b. Scanning electron microscope (SEM) and transmission electron microscope (TEM) images are shown in Fig. 1 and Fig. S3. The pristine WP shows a smooth surface with some individual particles on the surface, while pristine MoP and CoP exhibit porous nanostructures. Therefore, Mo or Co dopants might increase the porosity of WP. Fig. 1a1 and 1b1 show the SEM images of Mo-WP and Co-WP with porous microstructures. Specifically, Mo-WP is composed of nanoparticles (NPs) and Co-WP is composed of short nanorods (NRs). Compared with pristine WP, the surfaces of the M-WP nanomaterials are much rougher and exhibit abundant pores and closely interconnected networks, which could expose more active sites and enhance mass transport during the reaction process [23,38]. TEM images of Mo-WP and Co-WP are shown in Fig. 1. The observed lattice fringes on both Mo-WP and Co-WP are ca. 0.29 nm, corresponding to the (011) plane of WP (shown in Fig. 1a3 and b3). Meanwhile, no lattices assigned to MoP or CoP are observed, which is consistent with XRD results [39]. The energy-dispersive X-ray spectroscopy (EDS) mapping images of Mo-WP are shown in Fig. 1a4, revealing uniform distributions of Mo, W and P in Mo-WP and suggesting a homogeneous incorporation of Mo into WP. Similarly, Co-WP also shows uniform distributions of Co, W and P

(shown in Fig. 1b4). It should be noted that the theoretical metal dopant atomic percentage (at%) is 5 at% Mo-WP and 5 at% Co-WP, which is in accordance with that of the precursors. Moreover, the ICP-OES results reveal that the exact metal percentage of Mo/Co is close to the ratios of the precursors (shown in Table S1), indicating the quantitative control of the dopants. The low-temperature nitrogen adsorption-desorption isotherms of different samples are shown in Fig. S4a. As shown in Table S1, Mo-WP and Co-WP show much higher BET surface areas ($104.8 \text{ m}^2 \text{ g}^{-1}$ and $68.2 \text{ m}^2 \text{ g}^{-1}$, respectively) than the undoped WP ($13.5 \text{ m}^2 \text{ g}^{-1}$). The Barrett – Joyner – Halenda (BJH) method is used to calculate the pore size distribution. Mo-WP and Co-WP show mesoporous nanostructures with average pore diameters of ca. 4.3 nm and 4.9 nm, respectively (shown in Fig. S4b and S4c). The surface area and pore size results further confirm the porous nanostructures of M-WP nanomaterials. The high surface areas and porous nanostructures of M-WP should expose more active sites and enhance mass transfer, which could facilitate the HER kinetics.

3.2. HER activities of the catalysts over wide pH range

HER activities of Mo-WP and Co-WP were measured in 1.0 M KOH. For comparison, glassy carbon electrodes (GCEs) were also modified with other pristine phosphides and commercial 20 wt% Pt/C (Alfa Aesar). Fig. 2a shows the polarization curves of the tested samples. At the current density of -10 mA cm^{-2} , the overpotentials of Co-WP and Mo-WP were -119 mV and -175 mV , respectively, significantly lower than those of pristine WP (-261 mV), MoP (-252 mV) and CoP (-289 mV). Tafel slopes were then calculated to reveal the inherent property of HER and verify the mechanism. Co-WP and Mo-WP exhibited Tafel slopes of ca. 55 mV/dec and 75 mV/dec , respectively, which were much smaller than those of un-doped TMPs (shown in Fig. 2b). The Tafel slopes suggested a Volmer-Heyrovsky reaction pathway on Co-WP and Mo-WP. The stabilities of the samples were measured by cycling the Co-WP and Mo-WP electrodes for 2000 cycles (shown in Fig. S5a1 and S5b1). The i-V curves of Co-WP and Mo-WP remained similar to the initial cycles with negligible loss in the cathodic current. Moreover, the cathodic currents of Co-WP and Mo-WP at fixed overpotentials remained at ca. -10 mA cm^{-2} over 10 h, further confirming the excellent stability of the Co-WP and Mo-WP electrocatalysts in alkaline electrolytes. Specifically, the performance of Co-WP is among the best reported TMP-based catalysts for alkaline HER (shown in Table S2).

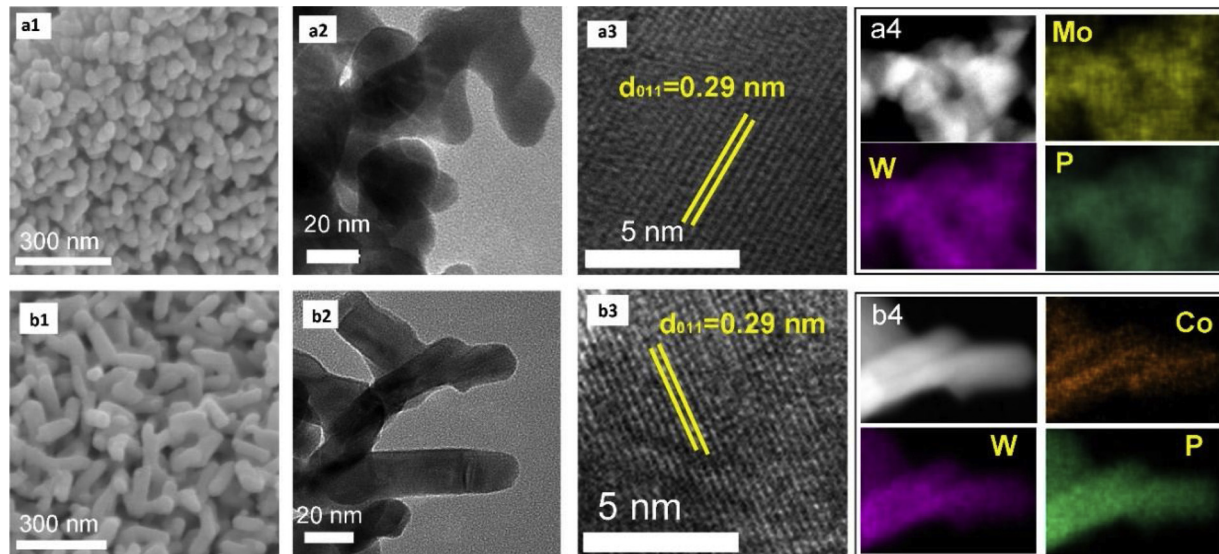


Fig. 1. (a1, b1) SEM images, (a2, b2) TEM images, (a3, b3) HRTEM images and (a4, b4) STEM-EDS mappings of W, P, Mo and Co of Mo-WP and Co-WP nanomaterials.

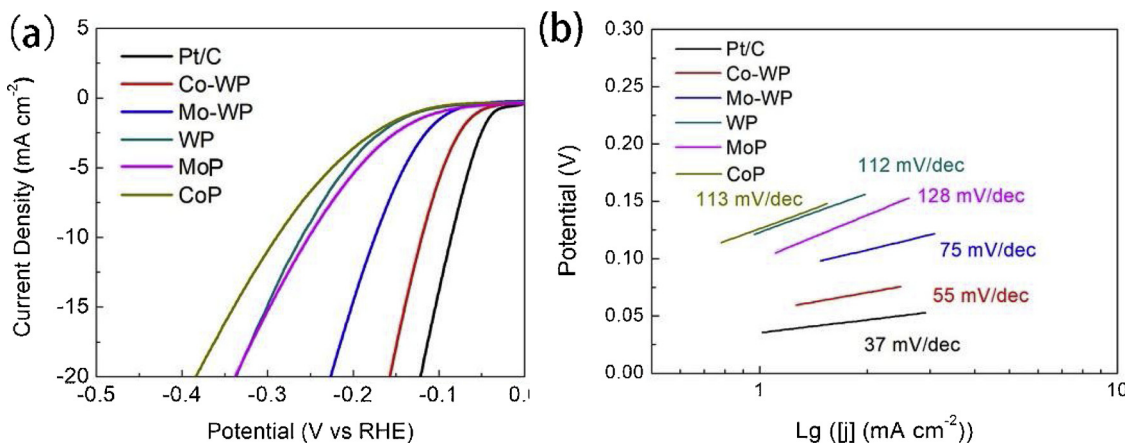
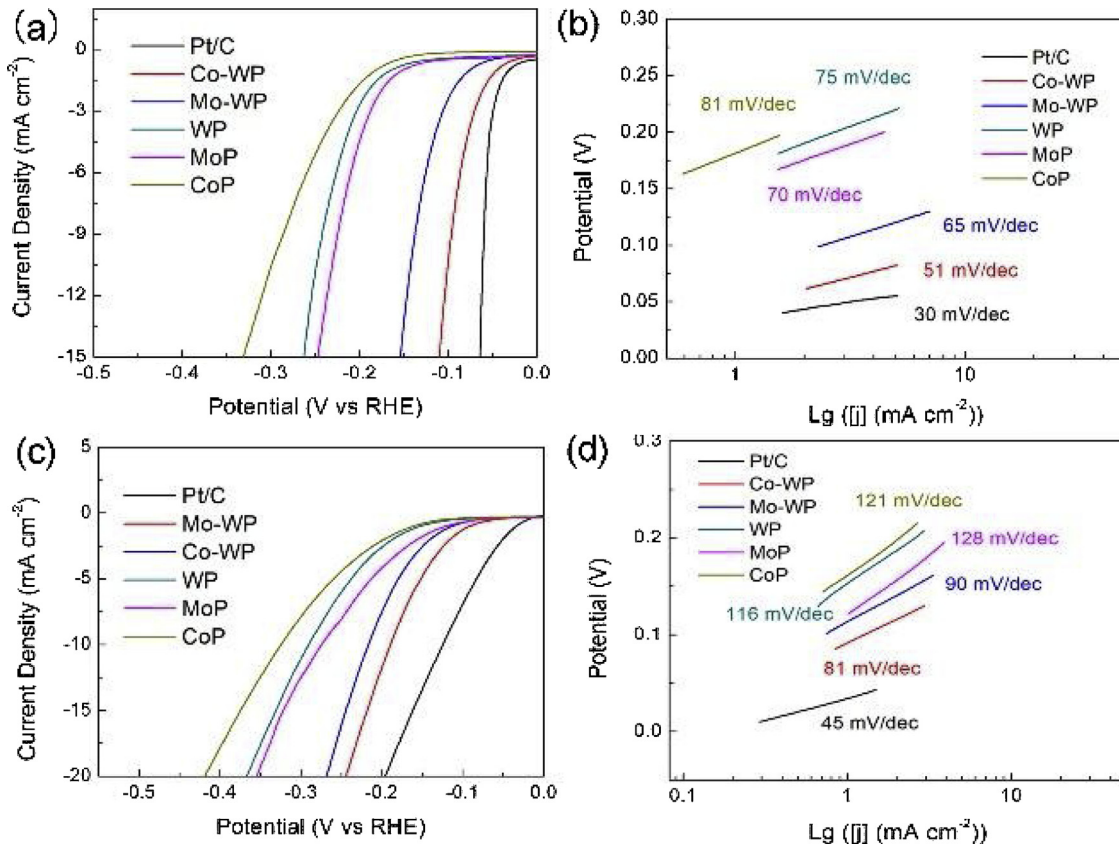


Fig. 2. (a) HER polarization curves and (b) Tafel plots of different samples in 1 M KOH.

Fig. 3. HER polarization curves and Tafel plots of different samples in (a, b) 0.5 M H_2SO_4 and (c, d) 1 M PBS electrolytes.

The as-prepared samples were then tested in 0.5 M H_2SO_4 and 1 M phosphate buffer saline (PBS). In 0.5 M H_2SO_4 , the overpotentials at -10 mA cm^{-2} of Co-WP (-98 mV) and Mo-WP (-139 mV) were much smaller than those of pristine WP (-197 mV), MoP (-228 mV) and CoP (-295 mV) (shown in Fig. 3a). Moreover, the obtained Tafel slopes of Co-WP (51 mV/dec) and Mo-WP (65 mV/dec) were significantly smaller than those of the pristine phosphides (shown in Fig. 3b). Fig. S5a2 and S5b2 show that both Co-WP and Mo-WP exhibited good stabilities in 0.5 M H_2SO_4 . The acid HER performance of Co-WP is among the best reported TMP-based catalysts for acid HER (shown in Table S3). Fig. 3c and d show the HER performances of different samples in the neutral electrolyte (1 M PBS). Co-WP and Mo-WP required overpotentials of -189 mV and -216 mV , respectively, to reach the current density of -10 mA cm^{-2} , with Tafel slopes of 81 mV/dec and 90 mV/dec , respectively.

The relatively high overpotentials and Tafel slopes in 1 M PBS are likely due to the sluggish ion migration in PBS electrolyte and thus leading to the inherently slower kinetics [40]. However, the HER performances of Co-WP and Mo-WP were still much better than those of the pristine TMPs. Fig. S5a3 and S5b3 show that both Co-WP and Mo-WP exhibited high stabilities in 1 M PBS. Overall, the electrocatalytic results above demonstrated that Co-WP exhibited excellent HER activities and stabilities over wide pH range among the as-prepared samples in this work (shown in Table S4). Moreover, Co-WP also outperformed many reported metal phosphides over a wide pH range, as summarized in Table S5 and S6.

In order to compare the intrinsic area-specific activities of different samples, electrochemical double-layer capacitances (C_{dl}) of different samples were measured to determine the active surface areas and

estimate the density of electrochemically active sites [41–43]. As shown in **Fig. S6**, the C_{dl} s of Mo-WP (2.5 mF cm⁻²) and Co-WP (2.3 mF cm⁻²) were significantly higher than that of pristine WP (0.98 mF cm⁻²), suggesting that more active sites have been exposed. The LSV results were then calibrated with the values of ECSA. [44–46] As shown in **Table S7** and **S8**, the ECSA-normalized exchanged current density (J_0) and Tafel slope of M-WP outperformed the undoped WP, with Co-WP still exhibiting the best HER performance among catalysts in the current study. The intrinsic activities were evaluated by calculating the turnover frequency (TOF) for each sample [12,41–43]. As shown in **Fig. S8**, Co-WP exhibited significantly higher TOF than those of Mo-WP and pristine WP in different electrolytes, consistent with the trends of HER polarization curves. The AC impedance spectroscopy measurements were performed to investigate the HER reaction kinetics in acid and alkaline electrolytes (shown in **Fig. S9**). Both Co-WP and Mo-WP showed lower impedance values than pristine WP in both acid and alkaline electrolytes, which could enhance the charge transfer and consequently the HER rates [47,48]. In addition, the effects of doping percentages of Mo and Co toward HER activities are also investigated. As shown in **Fig. S10**, from 2.5 at% Mo/Co-WP to 10 at% Mo/Co-WP, the 5 at% Co-WP and 5 at% Mo-WP exhibit the best HER performance. The different activities might be due to changes in the number of active sites and charge transfer rates [7]. However, all the doped samples show better HER performance than the undoped samples, further confirming the promoting function of the dopants. Moreover, long-term HER electrolysis was also performed. As shown in **Fig. S11**, both Co-WP and Mo-WP showed good durability for 60 h HER tests over a wide pH range. Meanwhile, **Fig. S12** confirmed that these catalysts maintained their morphology and composition after the long-term stability test.

3.3. DFT calculations of the overall HER process

DFT calculations were performed to fundamentally understand the effect of metal dopants on the HER over Mo-WP, Co-WP and pristine WP. **Fig. S13** to **S15** show the detailed geometries and HER pathways of Co-WP, Mo-WP and WP. The WP (011) surface was modeled using a (4 × 4) three-layers unit slab with ~30 Å vacuum. One of W atoms in the top layer was replaced by a Mo (or Co) atom for Mo-doped (or Co-doped) WP models. Thus, the model gives a doping ratio of 6.25 at% Mo/Co on the surface, which is consistent with the experiments. The (011) surface was adopted due to the TEM characterization result. The hydrogen adsorption free energy (ΔG_{H^*}) has been widely reported as the key descriptor for HER activity in acid electrolytes [49,50]. The reaction pathways for HER for pristine WP and metal doped WP in acid electrolytes are shown in **Fig. 4a**. It could be observed that all three catalysts showed a negative ΔG_{H^*} . Therefore the lowest ΔG_{H^*} should

give the highest energy barrier for HER. Compared with the ΔG_{H^*} for WP (−0.72 eV), Mo-WP presents a slightly higher ΔG_{H^*} of −0.69 eV. In comparison, Co-WP significantly increases the ΔG_{H^*} to −0.48 eV, suggesting that Co doping could significantly improve the HER performance of WP in acid electrolytes.

However, in alkaline and neutral electrolytes, the energy barrier for water dissociation (ΔG_{H2O}^\ddagger) plays a key role in the entire HER reaction network and thus significantly governs the HER activity [17,51]. As shown in **Fig. 4b**, there are two steps representing an increasing free energy in the pathway, which could affect the activity for HER. The first is the water dissociation energy barrier, ΔG_{H2O}^\ddagger . The ΔG_{H2O}^\ddagger for pristine WP is 0.47 eV, and the Mo-WP presents a similar ΔG_{H2O}^\ddagger of 0.49 eV. In comparison, the Co-WP presents a lower ΔG_{H2O}^\ddagger of 0.40 eV, suggesting that the Co doping would benefit the water dissociation kinetically. Another energy barrier in the pathway shows in the step of H₂ production, with the corresponding energy noted as ΔG_H . The ΔG_H value for pristine WP is 0.34 eV while both Mo and Co doping could lower the energy, with ΔG_H being 0.29 eV for Mo-doped WP and 0.24 eV for Co-doped WP. Therefore, the Co doping can reduce both energy barriers for HER compared with WP, and Mo doping only presents a slightly better kinetics than pure WP. Namely, both water dissociation and hydrogen release are significantly accelerated on Co-WP. These results are consistent with the experimental observation of enhanced HER performances after metal doping (**Figs. 2 and 3**). Overall the DFT results suggest that metal dopants, especially Co doping, exhibit a coordinative effect of enhancing water dissociation and optimizing hydrogen adsorption, and consequently facilitate all of the HER steps in alkaline, acid and neutral solutions.

4. Conclusions

In summary, Mo and Co have been incorporated into WP using a metal doping strategy, leading to the formation of porous M-WP (M = Mo, Co) nanomaterials with enhanced HER performance over wide pH range. In particular, the efficient pH-universal HER performances of Co-WP and Mo-WP are owing to their advantageous structural and inherent properties. First, the porous nanostructures and high surface areas of M-WP (M = Mo, Co) should promote the mass transfer during HER. The increased electrochemical double-layer capacitances (C_{dl}) indicate that more active sites are exposed on M-WP. In addition, the decreased charge-transport impedance of M-WP also enhances the HER kinetics. Therefore, both Mo-WP and Co-WP exhibit enhanced HER performances than pristine WP. Second, DFT results specifically show that the water dissociation step and hydrogen generation step are both optimized after the Co doping. As a result, the HER rates of Co-WP should be further improved in comparison with Mo-WP. Owing to the

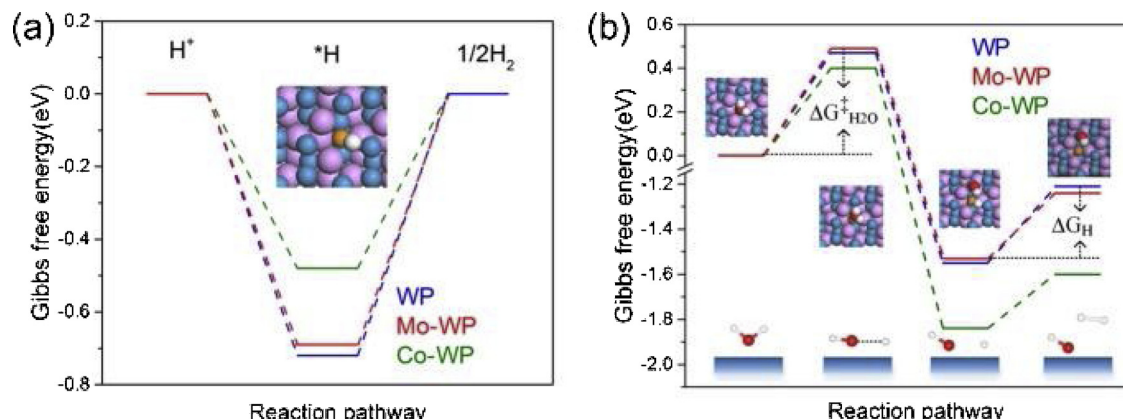


Fig. 4. DFT calculations of HER reaction pathways of pristine WP, Mo-WP and Co-WP in (a) acid electrolytes and (b) alkaline and neutral electrolytes. The structural models are the top views of the Co-WP. Co: orange, P: purple, W: blue, O: red and H: white (For interpretation of the references to colour in this figure legend, the reader is referred to the web version of this article).

advantages above, Co-WP exhibited significantly enhanced HER kinetics over wide pH range. The combined experimental and theoretical results provide insights in using transition metal doping strategy to fabricate non-precious metal catalysts with enhanced properties for electrochemical applications.

Acknowledgements

J. W. and K. C. contributed equally to this work. This work was supported by the National Key Research and Development Program of China (2016YFB0600902); National Natural Science Foundation of China (21536008 and 91334206); China Scholarship Council (201706250084 and 201706210117). We thank Prof. Tao Xue and Mr. Zhitao Zhang for their kind help during the revision.

Appendix A. Supplementary data

Supplementary material related to this article can be found, in the online version, at doi:<https://doi.org/10.1016/j.apcatb.2019.03.065>.

References

- [1] J.P. Liu, Y.Z. Liu, D.Y. Xu, Y.Z. Zhu, W.C. Peng, Y. Li, F.B. Zhang, X.B. Fan, *Appl. Catal. B* 241 (2019) 89–94.
- [2] F.Y. Cheng, J. Shen, B. Peng, Y.D. Pan, Z.L. Tao, J. Chen, *Nat. Chem.* 3 (2011) 79–84.
- [3] H. Lv, X. Chen, D.D. Xu, Y.C. Hu, H.Q. Zheng, S.L. Suib, B. Liu, *Appl. Catal. B* 238 (2018) 525–532.
- [4] H.J. Tang, C.M. Hessel, J.Y. Wang, N.L. Yang, R.B. Yu, H.J. Zhao, D. Wang, *Chem. Soc. Rev.* 43 (2014) 4281–4299.
- [5] Q. Lu, G.S. Hutchings, W.T. Yu, Y. Zhou, R.V. Forest, R.Z. Tao, J. Rosen, B.T. Yonemoto, Z.Y. Cao, H.M. Zheng, J.Q. Xiao, F. Jiao, J.G. Chen, *Nat. Commun.* 6 (2015) 6567–6574.
- [6] J.A. Turner, *Science* 305 (2004) 972–974.
- [7] X. Zhong, Y.Y. Sun, X.L. Chen, G.L. Zhuang, X.N. Li, J.-G. Wang, *Adv. Funct. Mater.* 26 (2016) 5778–5786.
- [8] L.S. Peng, X.Q. Zheng, L. Li, L. Zhang, N. Yang, K. Xiong, H.M. Chen, J. Li, Z.D. Wei, *Appl. Catal. B* 245 (2019) 122–129.
- [9] C. Yang, M.Y. Gao, Q.B. Zhang, J.R. Zeng, X.T. Li, A.P. Abbott, *Nano Energy* 36 (2017) 85–94.
- [10] S.K. Kim, Y. Qiu, Y.-J. Zhang, R. Hurt, A. Peterson, *Appl. Catal. B* 235 (2018) 36–44.
- [11] S.H. Guo, X.H. Li, X.G. Ren, L. Yang, J.M. Zhu, B.Q. Wei, *Adv. Funct. Mater.* 28 (2018) 1802567.
- [12] J.J. Wang, W. Wang, Z.Y. Wang, J.G. Chen, C.-J. Liu, *ACS Catal.* 6 (2016) 6585–6590.
- [13] Y. Zheng, Y. Jiao, A. Vasileff, S.-Z. Qiao, *Angew. Chem. Int. Ed.* 57 (2018) 7568–7579.
- [14] L.S. Zhang, J.J. Lu, S.B. Yin, L. Luo, S.Y. Jing, A. Brouzgou, J.H. Chen, P.K. Shen, P. Tsakarous, *Appl. Catal. B* 230 (2018) 58–64.
- [15] Z.H. Pu, I.S. Amiinu, Z.K. Kou, W.Q. Li, S.C. Mu, *Angew. Chem. Int. Ed.* 129 (2017) 11717–11722.
- [16] H. Wang, S.X. Min, Q. Wang, D.B. Li, G. Casillas, C. Ma, Y.Y. Li, Z.X. Liu, L.-J. Li, J.Y. Yuan, M. Antonietti, T. Wu, *ACS Nano* 11 (2017) 4358–4364.
- [17] K. Xu, H. Ding, M.X. Zhang, M. Chen, Z.K. Hao, L.D. Zhang, C.Z. Wu, Y. Xie, *Adv. Mater.* 29 (2017) 1606980.
- [18] J.Q. Tian, Q. Liu, A.M. Asiri, X.P. Sun, *J. Am. Chem. Soc.* 136 (2014) 7587–7590.
- [19] D.Y. Chung, S.W. Jun, G. Yoon, H. Kim, J.M. Yoo, K.-S. Lee, T. Kim, H. Shin, A.K. Sinha, S.G. Kwon, K. Kang, T. Hyeon, Y.-E. Sung, *J. Am. Chem. Soc.* 139 (2017) 6669–6674.
- [20] Y. Ge, P. Dong, S.R. Craig, P.M. Ajayan, M. Ye, J. Shen, *Adv. Energy Mater.* 8 (2018) 1800484.
- [21] R. Wang, X.-Y. Dong, J. Du, J.-Y. Zhao, S.-Q. Zang, *Adv. Mater.* 30 (2018) 1703711.
- [22] C. Tang, L.F. Gan, R. Zhang, W.B. Lu, X. Jiang, A.M. Asiri, X.P. Sun, J. Wang, L. Chen, *Nano Lett.* 16 (2016) 6617–6621.
- [23] Z.C. Xing, Q. Liu, A.M. Asiri, X.P. Sun, *Adv. Mater.* 26 (2014) 5702–5707.
- [24] Z.H. Pu, Q. Liu, A.M. Asiri, X.P. Sun, *ACS Appl. Mater. Interfaces* 6 (2014) 21874–21879.
- [25] T.T. Liu, D.N. Liu, F.L. Qu, D.X. Wang, L. Zhang, R.X. Ge, S. Hao, Y.J. Ma, G. Du, A.M. Asiri, L. Chen, X.P. Sun, *Adv. Energy Mater.* 7 (2017) 1700020.
- [26] Z.H. Pu, X. Ya, I.S. Amiinu, Z.K. Tu, X.B. Liu, W.Q. Li, S.C. Mu, *J. Mater. Chem. A* 4 (2016) 15327–15332.
- [27] Z.C. Xing, Q. Liu, A.M. Asiri, X.P. Sun, *ACS Catal.* 5 (2015) 145–149.
- [28] J.M. McEnaney, J.C. Crompton, J.F. Callejas, E.J. Popczun, C.G. Read, N.S. Lewis, R.E. Schaak, *Chem. Commun.* 50 (2014) 11026–11028.
- [29] S.J. Deng, F. Yang, Q.H. Zhang, Y. Zhong, Y.X. Zeng, S.W. Lin, X.L. Wang, X.H. Lu, C.-Z. Wang, L. Gu, X.H. Xia, J.P. Tu, *Adv. Mater.* 30 (2018) 1802223.
- [30] T. Kou, T. Smart, B. Yao, I. Chen, D. Thota, Y. Ping, Y. Li, *Adv. Energy Mater.* 8 (2018) 1703538.
- [31] Y. Zheng, Y. Jiao, Y.H. Zhu, L.H. Li, Y. Han, Y. Chen, A.J. Du, M. Jaroniec, S.Z. Qiao, *Nat. Commun.* 5 (2014) 3783.
- [32] D.-Y. Wang, M. Gong, H.L. Chou, C.-J. Pan, H.A. Chen, Y.P. Wu, M.-C. Lin, M.Y. Guan, J. Yang, C.-W. Chen, Y.-L. Wang, B.-J. Hwang, C.-C. Chen, H.J. Dai, J. Am. Chem. Soc. 137 (2015) 1587–1592.
- [33] G. Kresse, J. Furthmüller, *Comput. Mater. Sci.* 6 (1996) 15–50.
- [34] J.P. Perdew, K. Burke, M. Ernzerhof, *Phys. Rev. Lett.* 77 (1996) 3865–3868.
- [35] S. Grimme, *J. Comput. Chem.* 27 (2006) 1787–1799.
- [36] T.T. Liu, A.M. Asiri, X.P. Sun, *Nanoscale* 8 (2016) 3911–3915.
- [37] W. Gao, M. Yan, H.Y. Cheung, Z. Xia, X. Zhou, Y. Qin, C. Wong, J.C. Ho, C.-R. Chang, Y. Qu, *Nano Energy* 38 (2017) 290–296.
- [38] L. Liao, S. Wang, J. Xiao, X. Bian, Y. Zhang, M.D. Scanlon, X. Hu, Y. Tang, B. Liu, H.H. Girault, *Energy Environ. Sci.* 7 (2014) 387–392.
- [39] H.W. Man, C.-S. Tsang, M.-J. Li, J.Y. Mo, B.L. Huang, L.Y.S. Lee, Y.-C. Leung, *Appl. Catal. B* 242 (2019) 186–193.
- [40] J. Wang, F. Xu, H.Y. Jin, Y.Q. Chen, Y. Wang, *Adv. Mater.* 29 (2017) 1605838.
- [41] J.D. Benck, T.R. Hellstern, J. Kibsgaard, P. Chakthranont, T.F. Jaramillo, *ACS Catal.* 4 (2014) 3957–3971.
- [42] J. Kibsgaard, C. Tsai, K. Chan, J.D. Benck, J.K. Nørskov, F. Abild-Pedersen, T.F. Jaramillo, *Energy Environ. Sci.* 8 (2015) 3022–3029.
- [43] J.D. Benck, Z.B. Chen, L.Y. Kuritzky, A.J. Forman, T.F. Jaramillo, *ACS Catal.* 2 (2012) 1916–1923.
- [44] J.Q. Zhuo, M. Caban-Acevedo, H.F. Liang, L. Samad, Q. Ding, Y.P. Fu, M.X. Li, S. Jin, *ACS Catal.* 5 (2015) 6355–6361.
- [45] M.S. Faber, R. Dziedzic, M.A. Lukowski, N.S. Kaiser, Q. Ding, S. Jin, *J. Am. Chem. Soc.* 136 (2014) 10053–10061.
- [46] M. Caban-Acevedo, M.L. Stone, J.R. Schmidt, J.G. Thomas, Q. Ding, H. Chang, M. Tsai, J. He, S. Jin, *Nat. Mater.* 14 (2015) 1245–1251.
- [47] X. Long, G.X. Li, Z.L. Wang, H.Y. Zhu, T. Zhang, S. Xiao, W.Y. Guo, S.H. Yang, *J. Am. Chem. Soc.* 137 (2015) 11900–11903.
- [48] R. Wu, J. Zhang, Y. Shi, D. Liu, B. Zhang, *J. Am. Chem. Soc.* 137 (2015) 6983–6986.
- [49] Z.-F. Huang, J.J. Song, K. Li, M. Tahir, Y.-T. Wang, L. Pan, L. Wang, X.W. Zhang, J.-J. Zou, *J. Am. Chem. Soc.* 138 (2016) 1359–1365.
- [50] C. Zhang, Y. Huang, Y.F. Yu, J.F. Zhang, S.F. Zhuo, B. Zhang, *Chem. Sci.* 8 (2017) 2769–2775.
- [51] J. Zhang, T. Wang, P. Liu, Z.Q. Liao, S.H. Liu, X.D. Zhuang, M.W. Chen, E. Zschech, X.L. Feng, *Nat. Commun.* 8 (2017) 15437.